www.nature.com/scientificdata

scientific data

OPEN

DATA DESCRIPTOR

30-years (1991-2021) Snow Water Equivalent Dataset in the Po River District, Italy

Matteo Dall'Amico[1], Stefano Tasin[1], Federico Di Paolo[1], Marco Brian[2], Paolo Leoni[2], Francesco Tornatore[2], Giuseppe Formetta[3], John Mohd Wani[4] ✉, Riccardo Rigon[3,4] & Gaia Roati[2,4]

This paper presents a long-term snow water equivalent dataset in the Po River District, Italy, spanning from 1991 to 2021 at daily time step and 500 m spatial resolution partially covering the mountain ranges of Alps and Apennines. The data has been generated using a hybrid modelling approach integrating the hydrological modelling conducted with the physically-based GEOtop model, preprocessing of the meteorological data, and assimilation of *in-situ* snow measurements and Earth Observation snow products to enhance the quality of the model estimates. A rigorous quality assessment of the dataset has been performed at different control points selected based on reliability, quality, and territorial distribution. The point validation between simulated and observed snow depth across control points shows the accuracy of the dataset in simulating the normal and relatively high snow conditions, respectively. Additionally, satellite snow cover maps have been compared with simulated snow depth maps, as a function of elevation and aspect. 2D Validation shows accurate values over time and space, expressed in terms of snowline along the cardinal directions.

Background & Summary

Snow is a critical component of the mountain cryosphere, playing a significant role in shaping the hydrology and climate dynamics[1,2]. As an essential interface between the Earth's surface and the atmosphere, snow influences other cryospheric elements, such as glaciers and permafrost[3]. The snowpack functions as a vital water reservoir, accumulating during winter and gradually releasing water during the melt season, thereby sustaining downstream water demands[1,4,5]. However, snow is highly sensitive to climate change, particularly in low- and mid-elevation mountain regions[1]. Changes in snow occurrence, melt timing, and variability can directly affect water availability in snowfed basins, with significant implications for both ecosystems and human populations[1].

In Europe, most river basins originate in the Alps, often referred to as the "water tower of Europe"[4]. In the Alps, snow is an important cryospheric component, playing an essential role in meeting the agricultural, domestic and industrial water needs in the lowlands[1,2]. Generally, the amount of water stored in a snowpack is defined in terms of snow water equivalent (SWE), i.e., the equivalent amount of water that would result after melting the entire snowpack. Thus, a question arises: "how much snow is stored in a particular basin and when will it melt?" This question is generally asked by public and private institutions that manage and monitor the water resources within a river basin. Additionally, another question in the context of ongoing climate change is usually posed by decision and policy makers who want to compare the current situation with the past: "is the snow content in a basin higher or lower with respect to the historical average?" Unfortunately, the significant spatio-temporal variability of snow remains a primary uncertainty[3] in assessing the amount of water available in a basin. Furthermore, the network of point-scale snow depth observations, although important for the snow monitoring, is not sufficient to obtain a thorough understanding of SWE in the territory because of the heterogeneity of the terrain[6], lack of representation in space,[7] and measurements of snow density[8]. This underscores the need for a long-term and spatial SWE dataset to understand the availability of water resulting from the melting of the snowpack to retrieve possible future scenarios, from the analysis of the recent past climate. Different studies have been recently addressed to the reconstruction of the past snow evolution over the Alps, in particular:

[1]Waterjade Srl, Pergine Valsugana Trento, Italy. [2]Po River Basin District Authority (AdBPo), Parma, Italy. [3]Department of Civil, Environmental and Mechanical Engineering, University of Trento, Trento, Italy. [4]C3A - Center Agriculture Food Environment, University of Trento, San Michele all'Adige, Trento, Italy. ✉e-mail: johnmohd.wani@unitn.it

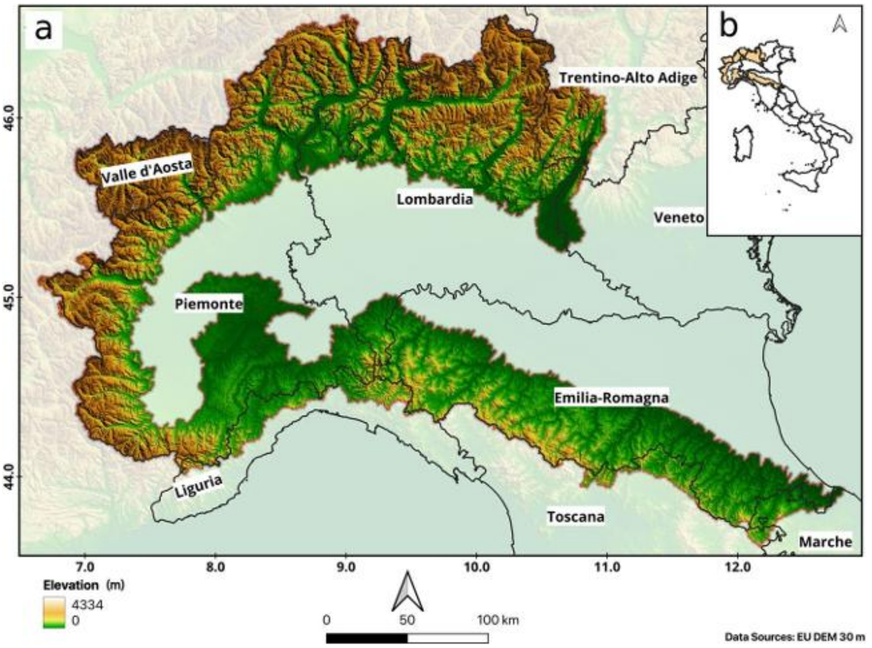

Fig. 1 (**a**) Topography of the study domain, i.e., the mountain part of the Po River District (Italy). (**b**) Location of the study domain on the map of Italy (yellow part, inset map).

(a) Avanzi *et al.*[9] performed an analysis of the precipitation lapse rate over the Western Europe Alps in the years 2008-2019; (b) Avanzi *et al.*[10] provided a reanalysis of snow evolution over the Italy in the period between 2010 and 2021 (recently extended to 2023), integrating physical modeling, *in-situ* data and satellite data; (c) Bozzoli *et al.*[11] performed an analysis of the snowfall variation pattern in selected sites over the Alps between 1920 and 2020; (d) finally, other type of data-driven methods have been recently tested in the U.S. from the downscaling of SWE data[12]. Moreover, recent extreme events[2,13,14] have attracted the attention of river basin authorities and other stakeholders in having the data to quantify and manage the availability of water in respective river basins. In response to this, the Po River Basin District Authority (AdBPo) in collaboration with Waterjade Srl has developed a high quality, long-term spatial SWE dataset covering the mountain part of the Po River District.

In this study, we present a long-term spatial SWE dataset in the Po River District (Fig. 1), the largest in Italy[13], considered as the second most sensitive area in Europe after the Rhone River basin[2,5]. Similarly to the IT-SNOW[10] data product, this dataset is generated using a hybrid modelling approach[6] and should not be confused with the *in-situ* observations which are much more scattered and are unevenly distributed. To check and maintain the data quality before post-processing, a two-step validation has been done using (a) a comparison with *in-situ* snow depth measurements, and (b) a comparison with snow cover data from Earth Observation (EO), correcting the simulations assimilating *in-situ* and EO data.

We believe that the dataset produced fills an important gap in the scientific understanding of the hydrology in the area, representing an unprecedented piece of information for many reasons: (a) it reports the longest time series of coherent SWE cartography at daily aggregation in Italy (Avanzi *et al.* dataset[10] covers the years 2010-2023); (b) the maps are, for what possible, homogeneous in terms of approach along the 30 years over the whole domain, facilitating the interpretation of results; (c) the maps can be interrogated to calculate the SWE anomaly of a given position, with respect to the statistical distribution of the same quantity during the period 1991-2021, thus helping to address drought alerts caused by missing snow[13,14]; (d) it can be used to validate temperature index models and other simple models, which are frequently used for practical purposes.

Methods

The spatial SWE dataset in the Po River District has been generated using a hybrid approach called J-snow[6], used in the last 10 years to support hydrological balances in different Italian alpine regions (https://aineva.it/wp-content/uploads/2019/12/NV93_2b.pdf). The modeling approach is built on the following procedures (see Fig. 2); (a) preprocessing of the meteorological data through the use of the MeteoIO library (https://meteoio.slf.ch/)[15]; (b) snow computation through GEOtop 2.0[16,17]; (c) assimilation of *in-situ* snow measurements; (d) assimilation of EO snow products. Finally, a tiling approach[18] has been used in order to efficiently manage the computational effort needed for the simulations.

Meteo data preprocessing.

The modelling chain has been driven using the following inputs (see Fig. 2): (a) meteorological data (i.e., air temperature, precipitation, direct shortwave radiation, wind velocity, air humidity) available at different locations within the computational domain, properly validated and homogenized. These data have been provided by various environmental agencies and government bodies located in the northern Italy and surrounding countries (see Acknowledgments for a full reference and their availability); (b) ERA5-Land[19] meteorological reanalysis data, used to integrate those areas and years where *in-situ* meteo data

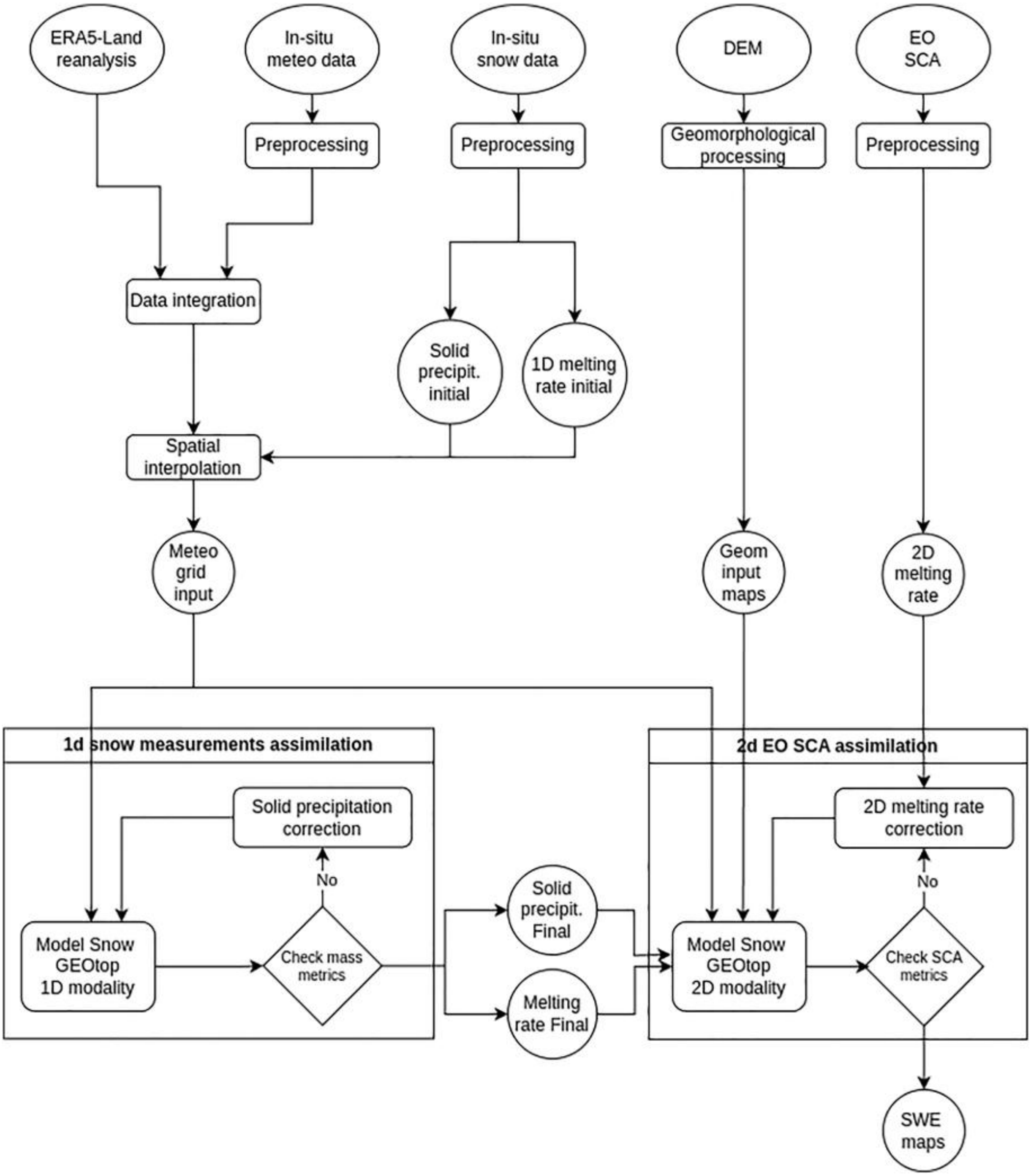

Fig. 2 Flow chart showing the modelling chain used to generate the data.

was not available (https://cds.climate.copernicus.eu/datasets/reanalysis-era5-land?tab=overview); (c) point snow depth (HS) data, at automatic and manual stations, collected from various avalanche warning agencies (see Acknowledgments for a full reference), integrated with the HS dataset produced by Matiu *et al.*[20] (https://doi.org/10.5281/zenodo.4064128); (d) Snow Cover Area (SCA) maps generated from MODIS data produced by Eurac Research[21,22] available since the 2002-2003 winter season and having a 250 m spatial resolution (https://edp-portal.eurac.edu/discovery/ed636c24-24b3-11ef-9957-8d8b4d692a59); (e) a Digital Elevation Model (DEM) having a 500 m resolution[23], necessary to create the geomorphological input maps for the physical model (https://cis2.eea.europa.eu/data/260/).

As *in-situ* meteorological records are often affected by quality[24], reliability or representativeness issues[7], the following processing procedures have been applied: (a) data cleaning, (b) calculation of the cloud transmittance, (c) gap filling of meteo data, (d) spatial interpolation of meteorological variables.

Meteo variable	TA	PSUM	RH	VW	ISWR	P	HS	TAU_CLD
Filter								
MIN_MAX	✓	✓	✓	✓	✓	✓	✓	
RATE	✓						✓	
UNHEATED_RAINGAUGE		✓						
DESPIKING							✓	
UNDERCATCH_WMO		✓						
Generator								
TAU_CLD								✓
1D Interpolation algorithm								
LINEAR								✓
2D Interpolation algorithm								
IDW_LAPSE	✓	✓		✓				
LISTON_RH			✓					
STD_PRESS						✓		
IDW								✓
Trend algorithm								
RATE	✓							
FRAC		✓		✓				

Table 1. Filters, processing and interpolation algorithms available in the MeteoIO library used for the meteorological variables. (TA: air temperature, PSUM: water equivalent of precipitations, either solid or liquid, RH: relative humidity, VW: wind velocity, ISWR: incoming short wave radiation, P: air pressure, HS: height of the snow, or snow depth, TAU_CLD: cloud transmissivity; MIN_MAX: imposes minimum and maximum limits on meteorological data values, removing or limiting those that fall outside these realistic ranges. RATE: checks the rate of change between consecutive data points, identifying and correcting changes that are too rapid, which may indicate sensor errors. UNHEATED_RAINGAUGE: correcting data from unheated rain gauges, which can be unreliable in freezing conditions. DESPIKING: removes sudden, anomalous spikes in the data, often caused by sensor malfunctions or electronic noise. UNDERCATCH_WMO: corrects the underestimation of precipitation by applying guidelines from the World Meteorological Organization (WMO), particularly in windy or snowy conditions, IDW: Inverse Distance Weighting, IDW_LAPSE: IDW by incorporating a lapse rate, LISTON_RH: implements a method for spatial interpolation of RH, STD_PRESS: calculates standard atmospheric pressure as a function of the elevation, RATE: Calculate the change rate, i.e, slope between two points, FRAC: fractional.).

Data cleaning, includes the application of different filters for the meteorological variables[24,25] that help to remove the noise from the data and ensure the integrity. We used the filters provided in the MeteoIO library[15]; in particular, Table 1 reports a list of the filters, processing and interpolation algorithms applied for each meteorological variable, namely, air temperature (TA), water equivalent of precipitations, either solid or liquid (PSUM), relative humidity (RH), wind velocity (VW), incoming short wave radiation (ISWR), air pressure (P), height of the snow, or snow depth (HS), cloud transmissivity (TAU_CLD). In the MeteoIO library, the MIN_MAX filter imposes minimum and maximum limits on meteorological data values, removing or limiting those that fall outside these realistic ranges. The RATE filter checks the rate of change between consecutive data points, identifying and correcting changes that are too rapid, which may indicate sensor errors. UNHEATED_RAINGAUGE is a specific filter for correcting data from unheated rain gauges, which can be unreliable in freezing conditions. The DESPIKING filter removes sudden, anomalous spikes in the data, often caused by sensor malfunctions or electronic noise, while UNDERCATCH_WMO corrects the underestimation of precipitation by applying guidelines from the World Meteorological Organization (WMO), particularly in windy or snowy conditions[26]. To fill temporal gaps in the data, a linear interpolation is applied, but only for limited periods of missing data and depending on the specific variable; this approach ensures that the interpolation remains reliable, avoiding excessive assumptions over long gaps.

Calculation of the cloud transmittance from direct shortwave radiation data, a necessary input for the GEOtop model, has been obtained using the TAU_CLD generator present in the MeteoIO library.

Meteo data spatial gap-filling, a common problem in meteorological time series and observational networks[27], has been done through a spatial interpolation of ERA5-Land data considering a 12 km radius around each measurement point. If no weather station is available within this radius, the centroid of the ERA5-Land cell is taken to create a virtual station. At this virtual station, we extract all the meteorological variables that are consistent with the *in-situ* data. Figure 3 shows the location of ERA5-Land centroids (blue circles) and *in-situ* stations (orange circles) in each tile of the computational domain, giving rise to a final homogeneous input in terms of spatial granularity. In case of neighbouring measurements of HS and daily manual measurements of HS (HS24), the priority has been given to the latter.

Tables 2, 3, 4 report the number of sensors (for each meteo variable, where HS24 and HN24 are daily manual measurements of HS and fresh snow, respectively) used as input for the physical model in every tile, averaged over each decade. It is noticeable the increase in the number of sensors during the second and the third decade;

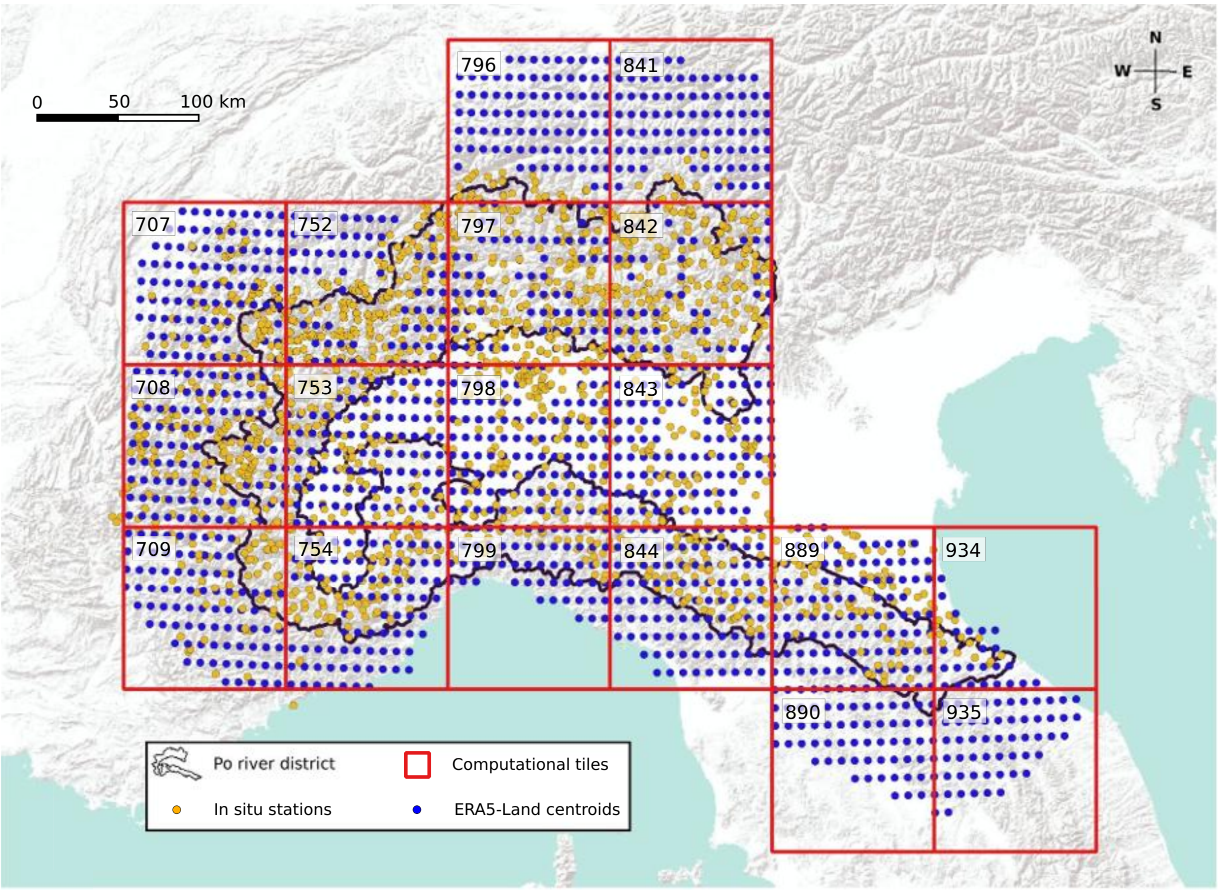

Data Sources: ESRI terrain

Fig. 3 Location of ERA5-Land centroids (blue circles) and *in-situ* stations (orange circles) used as input for the physical model. Computational tiles, with the identification number, are highlighted by the red grid.

Decade 1991-2000									
Tile	**HN24**	**HS**	**HS24**	**ISWR**	**P**	**PSUM**	**RH**	**TA**	**VW**
707	0	3	4	3	3	2	4	5	4
708	0	0	12	0	0	0	0	0	0
709	0	0	11	0	0	0	0	0	0
752	8	5	18	4	5	5	8	10	9
753	0	0	7	0	0	1	0	1	0
754	0	0	9	0	0	0	0	0	0
796	7	4	7	2	0	2	6	7	7
797	6	4	6	12	0	9	19	24	14
798	0	0	0	3	0	2	6	10	1
799	0	0	2	0	0	2	0	2	0
841	3	0	3	1	0	1	1	1	1
842	5	6	7	6	1	12	6	17	3
843	0	0	0	1	0	2	3	7	1
844	0	0	0	0	0	2	1	2	0
889	0	0	0	1	0	8	4	8	2
934	0	0	0	0	0	2	2	2	1

Table 2. Number of sensors used as input in each domain tile in the 1991-2000 decade. (HN24 and HS24 are daily manual measurements of snow height and fresh snow, respectively).

such increase is also highlighted in Table 5, where the total number of sensor per year and variable over the entire domain is reported.

Decade 2001-2010									
Tile	**HN24**	**HS**	**HS24**	**ISWR**	**P**	**PSUM**	**RH**	**TA**	**VW**
707	1	12	12	8	8	14	11	22	10
708	0	1	32	1	0	1	1	1	1
709	0	0	17	0	0	0	0	0	0
752	8	27	44	13	10	48	36	69	38
753	0	1	14	1	0	2	1	2	1
754	0	0	18	0	0	0	0	0	0
796	7	9	7	2	0	7	19	21	20
797	6	15	7	25	0	42	55	82	37
798	0	0	0	15	0	19	26	36	6
799	0	0	3	0	0	5	0	6	0
841	3	1	3	1	0	2	3	3	3
842	6	13	7	15	4	39	23	49	16
843	0	0	0	7	0	16	14	21	5
844	0	1	0	0	0	13	2	12	1
889	0	0	0	1	0	14	5	8	2
934	0	0	0	0	0	2	2	2	1

Table 3. Number of sensors used as input in each domain tile in the 2001-2010 decade.

Decade 2011-2021									
Tile	**HN24**	**HS**	**HS24**	**ISWR**	**P**	**PSUM**	**RH**	**TA**	**VW**
707	1	14	14	10	10	17	12	23	12
708	0	2	33	1	0	1	1	2	2
709	0	0	13	0	0	0	0	0	0
752	9	34	51	21	11	66	50	78	54
753	0	1	16	1	0	2	1	2	1
754	0	0	17	0	0	0	0	0	0
796	8	9	8	4	0	13	22	22	22
797	6	21	7	38	0	92	89	107	73
798	0	0	0	18	0	37	29	39	21
799	0	1	4	1	0	6	1	6	1
841	3	2	3	2	0	4	4	5	4
842	7	32	12	34	9	89	57	88	42
843	0	0	0	12	0	31	25	32	14
844	0	1	0	0	0	14	3	13	1
889	0	0	0	1	0	19	7	16	4
934	0	0	0	0	0	3	2	3	1

Table 4. Number of sensors used as input in each domain tile in the 2011-2021 decade.

Spatial interpolation of meteorological variables has been obtained using the Inverse Distance Weighting (IDW)[28] interpolation method present in the MeteoIO library. The algorithm performs spatial interpolation by weighting observations inversely to their distance from the target location. IDW_LAPSE enhances this by incorporating a lapse rate, adjusting interpolated values based on elevation differences, ideal for variables like temperature. When combined with a TREND of type GRAD (linear gradient) or FRAC (fractional), these methods account for broader spatial variations, refining the interpolation. The LISTON_RH algorithm implements a method for spatial interpolation of RH[29]. The process begins by calculating the dew point temperature for each input station, then dew point temperatures are spatially interpolated using the IDW_LAPSE algorithm. After the interpolation, the local dew point temperatures are converted back into relative humidity values. The STD_PRESS algorithm in MeteoIO calculates standard atmospheric pressure as a function of the elevation. It provides a baseline pressure estimate under standard conditions, mainly for correcting pressure-dependent meteorological variables; however, in GEOtop modeling, this has minimal impact modelling the snow. Table 1 reports the interpolation algorithms used for each meteo variable.

Snow processes model. GEOtop 2.0[16,17] is a process-based hydrological model that includes a multi-layer snow scheme for the efficient evolution of snowpack by solving 1D mass and energy balance[16], accounting for the physical processes affecting the snowpack such as compaction and melting. For the purpose of this work instead of using the full GEOtop model (i.e., water and energy balance), inclusive of the integration of Richards equation

Year	HN24	HS	HS24	ISWR	P	PSUM	RH	TA	VW
1991/1992	29	3	66	19	3	40	31	61	25
1992/1993	30	5	67	21	3	39	42	79	31
1993/1994	31	6	68	27	9	54	55	92	38
1994/1995	31	12	80	31	9	60	58	98	40
1995/1996	31	20	81	33	9	58	77	116	54
1996/1997	30	26	93	32	9	44	73	112	56
1997/1998	31	29	92	41	10	57	83	130	62
1998/1999	31	37	115	45	11	52	107	151	74
1999/2000	31	40	120	52	11	71	122	184	79
2000/2001	30	54	136	51	12	89	135	222	86
2001/2002	29	65	151	71	15	121	177	273	115
2002/2003	30	67	158	86	17	198	181	309	128
2003/2004	31	79	161	88	19	236	192	352	140
2004/2005	31	83	166	92	24	234	200	361	147
2005/2006	35	86	171	97	26	260	207	373	156
2006/2007	35	94	178	100	28	288	207	375	158
2007/2008	35	94	178	103	28	292	215	372	158
2008/2009	35	97	178	105	29	304	239	380	166
2009/2010	35	102	184	110	28	314	253	397	174
2010/2011	35	114	179	115	31	337	266	422	183
2011/2012	36	121	183	135	33	358	296	449	224
2012/2013	36	120	183	137	31	367	297	448	252
2013/2014	36	120	182	138	30	414	300	450	267
2014/2015	36	120	180	140	30	421	308	455	271
2015/2016	36	120	182	144	29	428	320	456	270
2016/2017	36	123	181	151	29	444	328	462	275
2017/2018	36	121	179	166	29	447	330	466	282
2018/2019	36	122	178	165	28	445	325	456	282
2019/2020	36	126	179	163	28	439	329	455	283
2020/2021	35	126	178	163	28	439	325	455	282

Table 5. Total number of sensors per meteo variable used as input for each hydrological year.

in 3D, only the energy balance has been used (i.e., the snow module), which is 1D and thus has no lateral transfer of energy or mass; in doing this, we were able to parallelise the computational burden in different machines without losing any representation of the physical processes[30]. In order to consider the morphological complexity of the terrain, responsible for the large snow heterogeneity in the mountains, the model is fed with geomorphological maps of elevation, slope, aspect and sky view factor. In configurations similar to the one used in this paper, GEOtop has been already used in literature to model the snowpack evolution on a basin scale[30–32]. No calibration of the snow parameters has been done, and the standard values reported in the literature have been considered as valid[31–34]. More information about the interpolation in GEOtop can be found in Appendix C of Endrizzi *et al.*[16].

Snow measurements assimilation.

The assimilation of snow gauge data is approached in two key ways: through mass correction of the precipitation amount and correction of the energy inflow.

Mass correction. Measuring precipitation at high elevations is challenging due to the problem of undercatch that may reach a 20%–50% reduction value in winter[35]. Several techniques are present to correct the undercatch error[36–38]. Stemming from the approach introduced by Mair *et al.*[39] we introduced a technique to transform the snow gauges time series into virtual rain measurements. We selected about 250 points across the domain (reported as orange circles in Fig. 4), based on criteria such as quality, territorial distribution and climate representativeness. Snow measurement time series have been filtered and processed in order to remove outliers and polish the signal. Then, analysing the HS signal, the various snowfall events along the time series have been identified and the corresponding volumetric amount of accumulation has been multiplied by the density of the fresh snow estimated through empirical formulations[40]. This activity requires a thorough match of simulations with the corresponding rain measurements to avoid false precipitation events and to estimate the actual snowfall elevation and amount. The procedure is recursively applied along all stations until an acceptable comparison between simulated and measured HS time series is reached (see "Validation" section); if the discrepancy between *in-situ* data and simulations passes a threshold-based check, the modeling exercise proceeds to satellite assimilation, otherwise a correction is calculated and applied in an iterative procedure. Finally, once obtained the final time series of solid precipitation along the various snow gauges, these are eventually used in the spatial interpolation procedure previously described to recalculate the final dataset of precipitation.

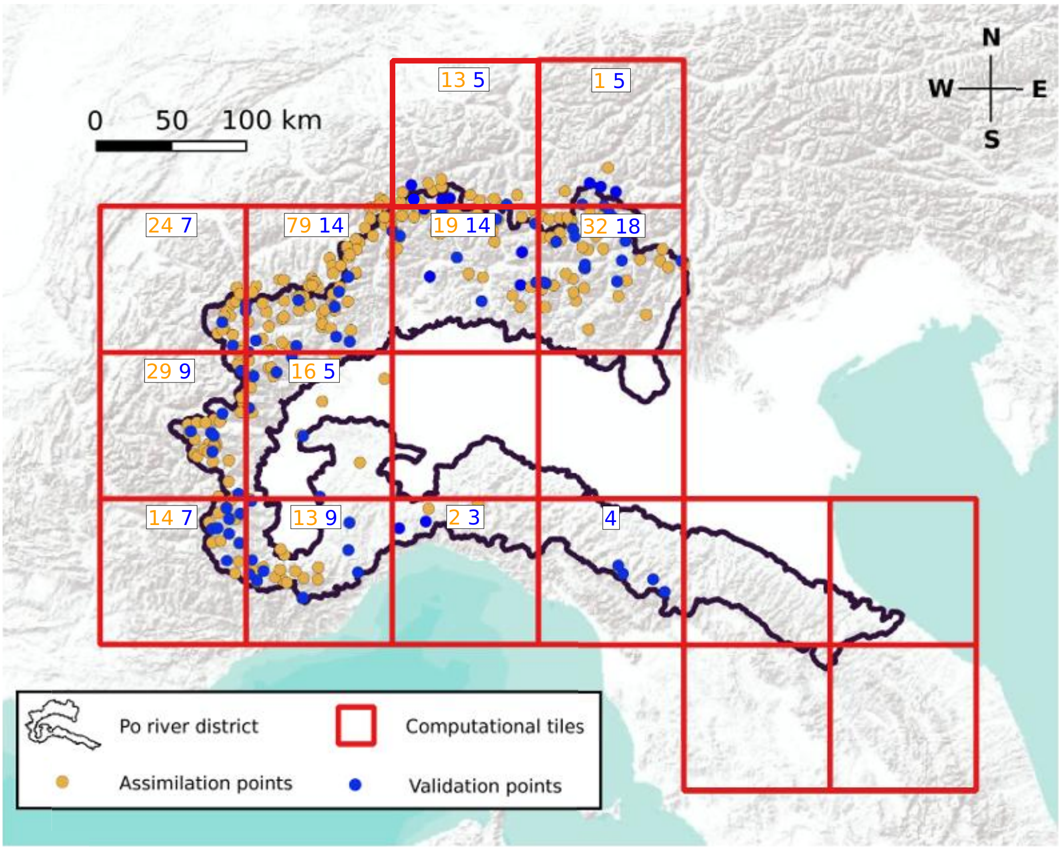

Data Sources: ESRI terrain

Fig. 4 Tiles used to computationally represent the Po River District (red grid). Points of HS assimilation and validation described in the "Validation" section are reported as orange and blue circles, respectively, with the total number in each tile reported with the same color.

Energy correction. Snow measurements are also used to correct the 1D melting rate simulated by the model to avoid either a too rapid or too slow snow melting rate. Such operation is done retrieving the melting rate on a single measurement point from the slope of the HS time series during a melting phase; the measured melting rate is then used to correct the 1D melting rate evaluated by the physical model. This procedure is performed over about 250 measurement points. Finally, interpolating these melting rate corrections considering the geomorphology of the area of interest, 2D melting rate correction maps are retrieved.

EO assimilation. After the evaluation of melting rate maps through the use of snow gauges data, MODIS-retrieved SCA maps are used for correcting the melting rate in 2D. In order to compare MODIS and simulated SCA, we used the so-called "*k* index", a metric that takes into account both the elevation and the aspect classes along the cardinal directions. This metric is used to efficiently evaluate the comparison of SCA between simulation and EO maps, enabling an iterative assimilation procedure. The goal of the comparison is not to exactly mimic the SCA evolution but to evaluate the representativeness of our results over the study area (expressed in terms of snowline along the cardinal directions), in coherence with geomorphological features such as aspect and elevation, i.e., the most important morphological features to explain the snow melting heterogeneity in the terrain.

The *k* index is based on the Intersection over Union (IoU), or Jaccard Index, a metric for comparing the similarity between two arbitrary shapes commonly used in computer vision[41,42] and also employed for classification of EO images[43,44]. For our application (i.e., an automatic assimilation of EO-retrieved SCA images to correct the melting rate when the discrepancy between EO images and simulated SCA exceeds a threshold), this index proves to be appropriate because it enables a quick comparison between the simulated and the MODIS-retrieved SCA over a peculiar plan, using the so-called radar plot. The radar plot represents the snowline as a function of cardinal directions at a global scale (see Fig. 5 for a graphic representation). The *k* index thus highlights the performance of the simulations in representing the snow melting process, expressed as snowline elevation, and triggers the correction of the melting rate as a function of both elevation and aspect.

Defining the union area (U) as the sum of the intersecting (I) and differing (D) SCA areas, the k index is expressed as the ratio of I over U (Fig. 5a):

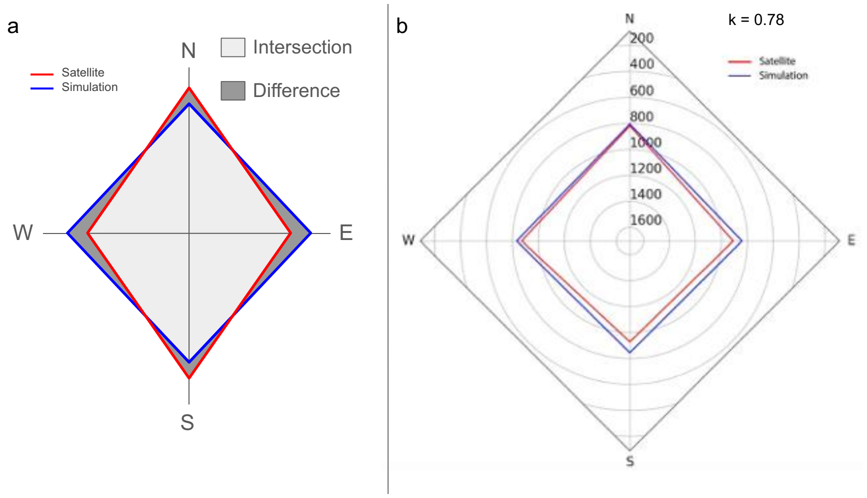

Fig. 5 (**a**) Illustration of intersection and difference between EO and simulated areas in the cardinal plane (i.e., the radar plot). (**b**) Example of a radar plot comparing EO-retrieved and simulated SCA images.

$$k = \frac{I}{U} = \frac{I}{(D + I)}. \tag{1}$$

For specific cases, some modifications to the original index were made. In particular, if both $I = 0$ and $D = 0$, (i.e., no snow on the terrain), no EO data assimilation is needed in the physical model. In such a case, the agreement between the EO image and the simulation is perfect, and k has been forced to be 1. Considering the extreme cases, in case of no intersection (i.e., $I = 0$), k will be equal to 0, whereas in case of no difference (i.e., $D = 0$), k will be equal to 1. For other values of I and D, k ranges between 0 and 1.

During the EO SCA assimilation procedure, a radar plot is generated (Fig. 5b) for each pair of corresponding images (simulation vs MODIS) to visualize differences in SCA across cardinal directions, offering a means to understand the value of the obtained k index. If the k index is below a threshold, thus indicating a significant discrepancy, the model calculates and applies a correction of the melting rate in the next iteration of GEOtop model simulations. Otherwise, the modelling proceeds to the retrieval of SWE maps. Being used for the correction of the melting rate, the MODIS images have been assimilated (and similarly used for the validation) every five days (or multiple, in case of cloudy images), a value appropriate according to the evolution of the snowpack.

Computational approach. In our modelling approach, we had to deal with the daunting task of managing a huge spatial domain (about 74,000 km^2), fine spatial resolution (500 m) and a long (30 year, daily) temporal dataset. This results in computationally intensive simulations that demand substantial computational resources and efficient processing methods. Therefore, we employed the sophisticated tiling approach[18] to enhance the efficiency and scalability of our simulations, dividing the computational domain in 18 squared tiles (having a 100 km side length) in order to ease the simulation control and split the calculation burden over different machines (see Fig. 3). To effectively implement this approach, we adopted methods that address the problem of coherence across the tiles in 2D simulations. In particular, to maintain the coherence of the interpolated meteorological data across the tiles, a buffer zone (4 km wide) has been considered to ensure smooth transitions between adjacent tiles. Similarly, to maintain the coherence of melting rate maps, *in-situ* data have been interpolated following the same approach used for the meteorological data.

The dataset, consisting of 30 years of data with 273 GeoTIFF maps per year, occupies approximately 1.5 GB on disk due to Lempel-Ziv-Welch (LZW) compression. However, when decompressed and loaded into memory, each map requires significantly more space. Each map has a resolution of 999 × 659 pixels with a single band, where each pixel is stored as a 16-bit integer (*Int16*), requiring 2 bytes per pixel. The memory required for a single map is calculated as:

$$\text{Memory (in bytes)} = \text{Width} \times \text{Height} \times \text{Bytes per pixel} \times \text{Number of bands},$$

i.e.: $999 \times 659 \times 2 = 1316682$ bytes (~ 1.26 MB). For the entire dataset, the total memory required to load all maps is:

$$\text{Total Memory (in GB)} = \frac{1.26\ \text{MB} \times 273\ \text{maps/year} \times 30\ \text{years}}{1024\ \text{MB/GB}} \approx 10\ \text{GB}.$$

To efficiently handle this dataset and perform computations, a computer with a multi-core processor, such as an Intel Core i7/i9 or AMD Ryzen 7/9, is recommended to ensure sufficient computational power for managing large datasets and performing geospatial analyses. At least 16 GB of RAM is required, although 32 GB or more is preferable to allow for loading multiple maps into memory simultaneously without performance slowdowns, especially considering the estimated 10.54 GB memory requirement for the entire dataset. For storage, a Solid-State Drive (SSD) with at least 512 GB of available space is ideal for fast read/write speeds. While the compressed dataset occupies only 1.5 GB, additional space is necessary for intermediate files and computation outputs. A dedicated GPU is not required, as all necessary calculations can be efficiently performed using the CPU.

Assumptions and limitations. The modeling of SWE using GEOtop presents several limitations, such as: (i) the model does not account for wind-driven snow transport, avalanche dynamics or snow accumulation at the base of steep slopes. (ii) The density of fresh snow and the precipitation phase mainly depend on 2 m air temperature without considering the atmospheric temperature profile. Such limitations and the physical validity of results under these assumptions are further described in the GEOtop model's documentation[16]

Additional limitations stem from the data quality[24] of *in-situ* meteorological data as highlighted in "Meteo data preprocessing" section. The *in-situ* datasets suffer from quality issues, availability, etc., necessitating the integration of the reanalysis datasets like ERA5-Land dataset[45]; at the same time, these reanalysis datasets are not a substitute for local-scale meteorological conditions[24]. Geostatistical methods and filtering techniques used for interpolation can sometimes fail to adequately represent complex phenomena such as thermal inversions or the intricacies of wind fields, which influence the snowpack energy exchanges[29].

Finally, the main limitations related to data assimilation are the following: (i) the *in-situ* measurements provide only indirect estimates of SWE, as they are based on volumetric observations, and (ii) the assimilation of the energy balance is constrained, as it can only be calculated for specific points within the domain, making it difficult to spatialize—even with satellite-based observations. Despite these limitations, the error associated with modeling of SWE using our methodology remains within acceptable bounds as highlighted in the "Technical Validation" section.

Data Records

The dataset is available on zenodo[46] and is distributed under Creative Commons Attribution 4.0 International license (https://creativecommons.org/licenses/by/4.0/). This spatial dataset is distributed as daily over a period of 30 years from 1991 to 2021, beginning on October 3rd of each year up to July 1st of next year. The data is distributed in GeoTIFF format with a spatial resolution of 500 m by 500 m consistent with the European Environment Agency (EEA) reference grid (https://www.eea.europa.eu/en/datahub/datahubitem-view/3c362237-daa4-45e2-8c16-aaadfb1a003b). To give an overview of the spatial nature of the data, a randomly selected low (December 1st, 2020) and a high snow (January 1st, 2021) snapshot in the study domain is shown in Fig. 6.

Within the repository, the data is organised into folders labelled with corresponding years, such as, "1991_1992", which means within the particular folder, there are for example the data from October 3rd, 1991 to July 1st, 1992 and so on for the subsequent years. Moreover, each daily data file follows a consistent naming convention, such as SWE on October 3rd, 1991 is named as "SWE_1991-10-03.tif".

Technical Validation

Since the dataset is the result of a complex modeling approach that integrates different kinds of experimental data, a proper validation is necessary to ensure its quality, reliability, and suitability for any further use. Such a validation has been carried out both at point *in-situ* HS observation locations and in a 2D spatial domain using satellite-retrieved SCA. Furthermore, a regional analysis and a consistency analysis of the dataset has been conducted.

Point scale validation. The validation using the HS measurements at *in-situ* points allows the assessment of model performance regarding the accurate representation of snow processes (i.e., accumulation and ablation) at the point scale[38]. In order to evaluate the performance of a model, a number of statistical metrics such as Nash-Sutcliffe efficiency (NSE)[47], Root Mean Square Error (RMSE) and Kling-Gupta model efficiency (KGE)[48] exist in the literature. Different studies report these metrics to evaluate the simulation of SWE against the point measurements[38,49–51]. For this particular point validation exercise, we used the widely employed basic statistical metric for model evaluation[52], the RMSE, which represents the variability and bias together[50] as:

$$\text{RMSE} = \sqrt{\frac{1}{N}\sum_{i=1}^{N}(y_i - \hat{y}_i)^2} \tag{2}$$

where, y_i and $\hat{y}_i$ represents the measured and simulated values, respectively and N is the total number of observations. In the study domain, the RMSE value for each year has been evaluated at 100 checkpoints by comparing the simulated snow depth data with the ones measured throughout the entire snow season. Figure 4 reports the location and the number of the validation points in the domain tiles (blue circles); because of low elevation and/or poor data availability, in some tiles (located over the Padan Plain and the Appennines mountain range in the southern part of the Po River District) no point scale validation has been made. Figure 7 shows the comparison of HS time series in two locations for the 2013/2014 snowy winter (panels a and c) and the 2016/2017 dry winter (panels b and d), reporting also the RMSE averaged over the entire seasons.

We classified each winter season based on two criteria: (a) the RMSE, calculated as the average across stations below the 80th percentile, with a threshold of 15 cm considered acceptable; (b) RMSE_q80, which represents the RMSE for the station at the 80th percentile, with a slightly higher threshold of 20 cm deemed acceptable. While the general RMSE provides an overall assessment across all checkpoints, RMSE_q80 specifically targets checkpoints with higher snow mass accumulations. Table 6 presents both RMSE and RMSE_q80 values at the conclusion of the iterative 1D assimilation process. The RMSE values show minimal variability over the study

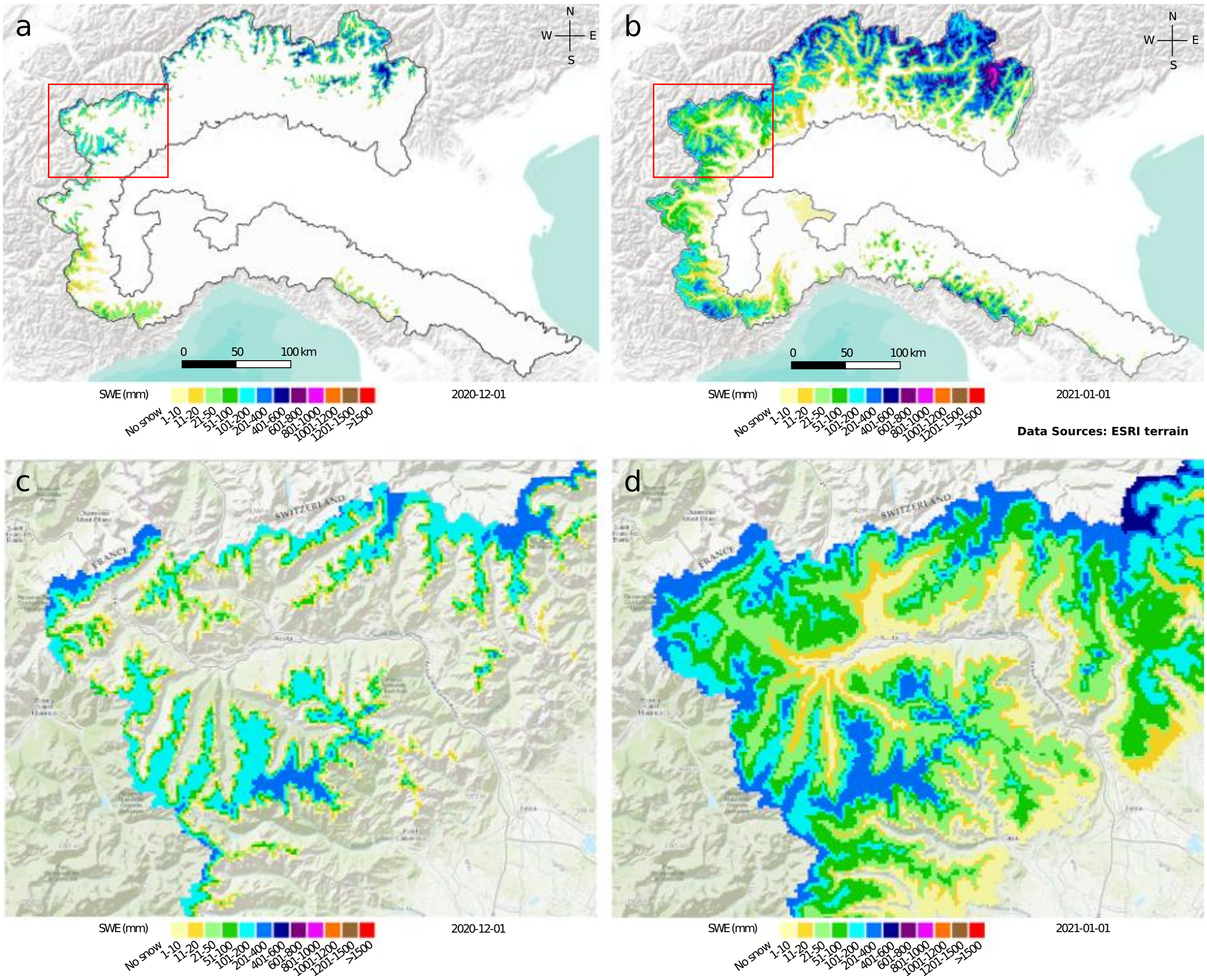

Fig. 6 The domain of the dataset in the Po River District showing SWE on December 1st, 2020 (**a**) and January 1st, 2021 (**b**). Panels (**c**) and (**d**) represent a zoom of the Valle d'Aosta Region (red box) in panels (**a**) and (**b**), respectively.

period, ranging between 6 to 15 cm, indicating that the modeling approach effectively simulates snow dynamics across all years. The RMSE_q80 values remain within the acceptable threshold for almost all years with only few exceptions, but the discrepancy with respect to the other years is poor. It's important to note that the RMSE values in Table 6 are averages from the entire snow gauge dataset, whereas the RMSE values in Fig. 7 pertain to specific validation points.

Spatial validation. Being an instantaneous observation of snow[53], satellite-derived SCA provide a reference to validate the modelling results. In this work, we used MODIS SCA maps as a benchmark, because of the accurate processing of MODIS images conducted by Notarnicola *et al.*[21]. The comparison of simulated and MODIS-retrieved SCA maps has been made considering different elevation and aspect classes. The satellite images classify pixels as snow covered (or snow free), therefore for such comparison, the simulated daily HS maps have been converted into binary SCA maps trivially using the threshold $HS > 0$ cm to retrieve binary values.

For the comparison between simulated and satellite-derived SCA, different types of evaluation metrics have been proposed in the literature[38,54]. For this work we used the k index defined in the "EO assimilation" subsection. Such metric is not addressed in verifying the correctness of our simulation only on a Cartesian 2D plane, but it is specifically used to evaluate the simulation performance (expressed as snowline identification) in terms of the geomorphological features of the terrain, i.e., aspect and elevation. In such a way, the metric does not report the accuracy of the simulation in terms of pixel classification (i.e., snow/snow free), but instead reflects the overall performance of the simulation based on both the EO image and the physical evolution of the SCA. It's worth noting that the values of the k index reported hereafter for data validation have been evaluated after the EO-SCA assimilation.

The quality of simulated SCA in terms of the k index has been evaluated in three dates, namely January 1st, March 1st and May 1st. In case of cloudy images, the subsequent date with a valid image has been considered. For each reference date, the k value is assessed in each tile and the average value across the entire study area is calculated, considering an average value of k=0.8 as acceptable. In Table 7, the k values representing an average

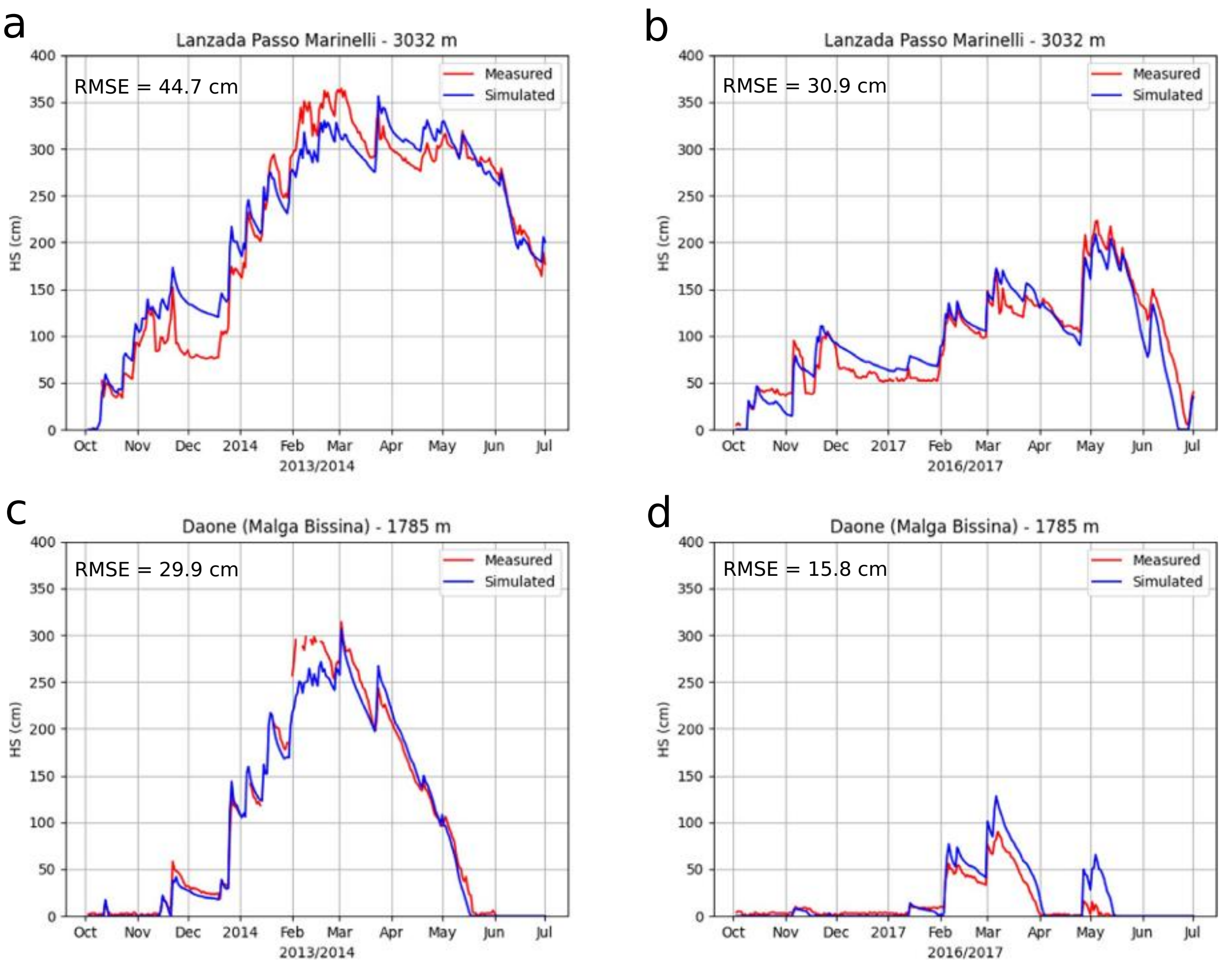

Fig. 7 Example of HS time series comparison in two stations over two winter seasons. The value of the RMSE is also reported. (**a**) Lanzada Passo Marinelli (3032 m) - 2013/2014; (**b**) Lanzada Passo Marinelli (3032 m) - 2016/2017; (**c**) Daone Malga Bissinia (1785 m) - 2013/2014; (**d**) Daone Malga Bissinia (1785 m) - 2016/2017.

of all *k* values over the tiles for the years considered (2002 onwards) are reported; *k* values are usually greater than 0.8, thus showing a good agreement between the model and satellite SCA.

Regional analysis. Considering the width of the area of interest, a regional analysis has been carried out to highlight the performance of the simulations in the different computational tiles. Such an analysis has been performed over two winter seasons that can be considered as opposites extreme cases: (a) the 2013/2014 very snowy winter, and (b) the 2016/2017 very dry winter. Figure 8 reports the tile-averaged values of RMSE (panels a and b) and RMSE_q80 (panels c and d) with respect to the HS time series over the winter seasons 2013/2014 and 2016/2017, respectively. Figure 9 reports the values of *k* over each tile at the check dates of January (panels a and b), March (panels c and d) and May (panels e and f) of 2014 and 2017, respectively. It's worth noting that for both the figures, averaging the values over the entire domain of simulation, the results reported in Tables 6 and 7, respectively, are obtained.

From Fig. 8, the following considerations can be taken: (a) As expected, RMSE and RMSE_q80 are higher for the snowy winter (2013/2014), because relative discrepancies between the simulated and the measured HS values have a higher absolute value, due the higher amount of snow; (b) RMSE and RMSE_q80 values show, as expected, a relation with the elevation; (c) only one tile (namely, 799) shows usually low values of the metrics because of the low snow content, nevertheless the values are comparable with the other tiles.

From Fig. 9, the following considerations can be taken: (a) *k* index shows high values (i.e., > 0.7) everywhere and for every check date (i.e., January, March and May), for both the winters; (b) higher *k* values are usually obtained over the Apennines (i.e., the mountain chain located in the southern part of the Po river basin), due to the lower amount of snow; (c) slightly lower *k* values are sometimes observed during May, when the melting takes place, and higher local differences in the SCA can be observed.

From the reported observations, we can consider our results coherent, having highlighted no tiles with low performance metrics over the two winters considered.

Year	RMSE (cm)	RMSE_q80 (cm)
1991/1992	10.0	16.3
1992/1993	9.8	17.5
1993/1994	11.6	19.2
1994/1995	10.1	18.2
1995/1996	10.7	16.8
1996/1997	11.2	18.1
1997/1998	10.3	16.5
1998/1999	11.5	18.8
1999/2000	8.4	15.8
2000/2001	10.8	17.8
2001/2002	6.7	14.5
2002/2003	8.9	16.8
2003/2004	11.8	19.5
2004/2005	9.5	16.7
2005/2006	11.1	18.0
2006/2007	6.4	14.0
2007/2008	11.0	18.7
2008/2009	14.9	20.9
2009/2010	13.2	20.9
2010/2011	11.9	20.3
2011/2012	10.9	20.6
2012/2013	12.9	21.2
2013/2014	13.2	20.6
2014/2015	10.6	18.8
2015/2016	10.1	18.0
2016/2017	9.3	15.8
2017/2018	13.2	21.2
2018/2019	9.2	18.4
2019/2020	10.5	18.9
2020/2021	10.2	16.8

Table 6. Annual average RMSE (cm) and RMSE_q80 (cm) on all the validation points in the study domain.

Year	January	March	May
2002/2003	0.90	0.91	0.92
2003/2004	0.93	0.76	0.91
2004/2005	0.63	0.65	0.93
2005/2006	0.78	0.84	0.89
2006/2007	0.88	0.91	0.91
2007/2008	0.87	0.92	0.92
2008/2009	0.74	0.90	0.89
2009/2010	0.79	0.81	0.91
2010/2011	0.85	0.81	0.87
2011/2012	0.87	0.90	0.93
2012/2013	0.85	0.90	0.91
2013/2014	0.93	0.95	0.91
2014/2015	0.93	0.92	0.93
2015/2016	0.81	0.91	0.91
2016/2017	0.92	0.95	0.94
2017/2018	0.89	0.92	0.95
2018/2019	0.94	0.86	0.94
2019/2020	0.95	0.96	0.92
2020/2021	0.79	0.90	0.92

Table 7. Mean k index values for simulated SCA across the study domain on selected dates (January 1st, March 1st, and May 1st) from 2002 onwards. The k index values represent the average of all k values across the domain's tiles.

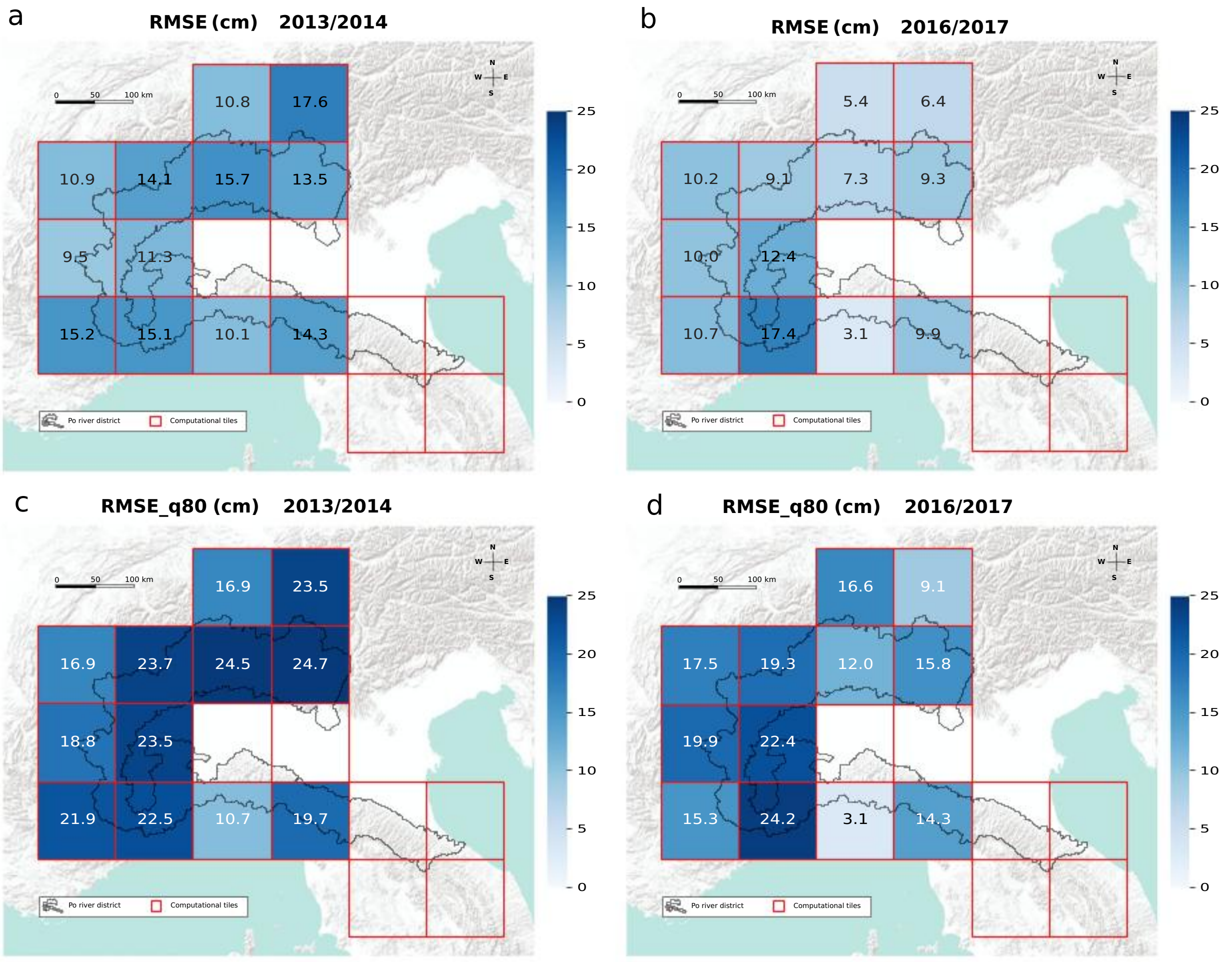

Data Sources: ESRI terrain

Fig. 8 Average HS RMSE and RMSE_q80 maps evaluated over each computational tile. The numbers report the same value of the scale color. (**a**) RMSE over the 2013/2014 winter. (**b**) RMSE over the 2016/2017 winter. (**c**) RMSE_q80 over the 2013/2014 winter. (**d**) RMSE_q80 over the 2016/2017 winter.

Dataset consistency. Since the assimilation of MODIS SCA images has been performed only for the years 2002-2021, a consistency check is necessary to ensure that there are no discontinuities in the dataset when compared to the years 1991-2002, during which no EO data were assimilated. This analysis focuses on evaluating the relative contributions of assimilating *in-situ* and EO data to the overall performance of the simulations. To quantify these contributions, a series of simulations were conducted with varying levels of input to the physical model: (a) Level 0, using only meteorological input; (b) Level 1, using meteorological input combined with the assimilation of EO SCA images; and (c) Level 2, using meteorological input along with the assimilation of both EO SCA images and *in-situ* snow gauge data. These simulations have been carried out for two distinct winters, the snowy 2013/2014 winter and the dry 2016/2017 winter, focusing on tiles 797 and 842, which encompass a mountainous area between the Lombardy and Trentino regions of Italy Table 8, Table 9.

Similar to the regional analysis discussed earlier, the results of the comparison analysis have been interpreted using two benchmarks:

- Snow gauges: The comparison between the simulations and the benchmark has been quantified as the average RMSE across the entire tile, considering all snow gauges (as detailed in the “Point Scale Validation” section). These results are presented in Table 8. In parallel with the RMSE (see Equation (2)), the Mean Absolute Error (MAE) for the HS time series has been also reported:

$$\mathrm{MAE}\ =\frac{1}{N}\sum_{i=1}^{N}|y_i-\hat{y}_i| \tag{3}$$

- EO-retrieved SCA: The comparison between the simulations and the benchmark has been assessed using the *k* index and the time series of the bias between EO-retrieved and simulated SCA. The results of this analysis are shown in Fig. 10. Furthermore, Table 9 reports the RMSE (% SCA) and MAE (% SCA) computed between

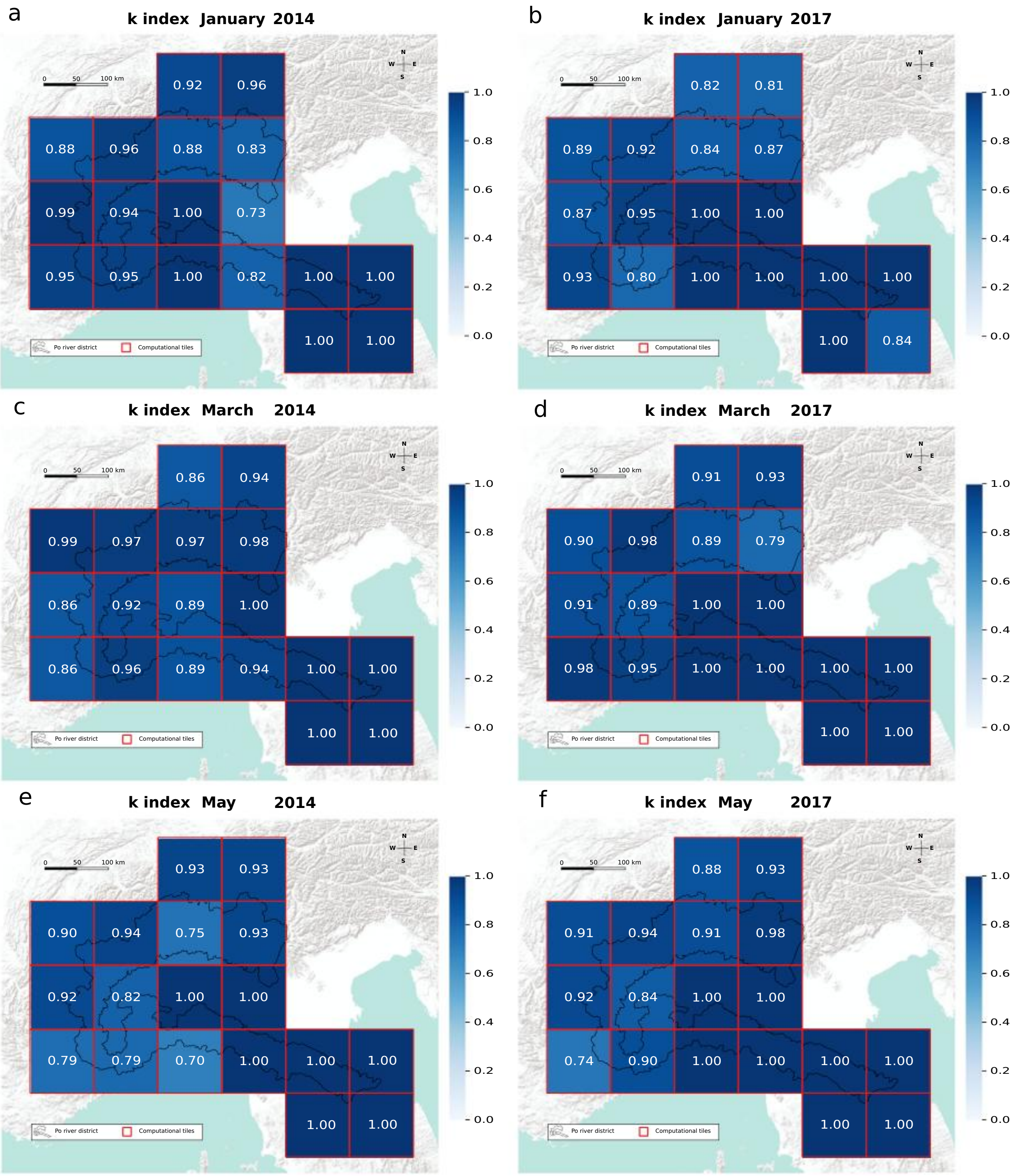

Data Sources: ESRI terrain

Fig. 9 *k* index on each computational tile at the check dates of: (**a**) January 2014; (**b**) January 2017; (**c**) March 2014; (**d**) March 2017; (**e**) May 2014; (**f**) May 2017.

the magenta (level 0), blue (level 1), and green (level 2) lines (all modeled) and the red line (EO observed) in Fig. 10.

Based on the data presented in Table 8, the following observations can be made:

1. RMSE and MAE values tend to be lower for the drier winter (2016/2017), consistent with the findings discussed in the previous section.
2. As expected, at the local scale Level 1 simulations (i.e., meteo input + EO data assimilation) yield results comparable to those obtained using only meteorological input, with some cases showing slight

		Simulation level					
		0		**1**		**2**	
		RMSE	**MAE**	**RMSE**	**MAE**	**RMSE**	**MAE**
797	**2013/2014**	62	52	61	52	50	40
	2016/2017	46	37	44	36	37	31
842	**2013/2014**	60	51	62	52	38	32
	2016/2017	30	25	32	27	22	18

Table 8. Average RMSE (cm) and MAE (cm) across an entire tile computed between modeled and simulate snow height as a function of tile, year and simulation level.

		Simulation level					
		0		**1**		**2**	
		RMSE	**MAE**	**RMSE**	**MAE**	**RMSE**	**MAE**
797	**2013/2014**	12	9	9	7	5	4
	2016/2017	12	9	11	8	6	5
842	**2013/2014**	15	12	12	10	7	6
	2016/2017	11	10	9	7	8	6

Table 9. RMSE (% SCA) and MAE (% SCA) computed between the modeled data (magenta, blue, and green lines) and the observed data (red line) in Fig. 9 as a function of tile, year and simulation level.

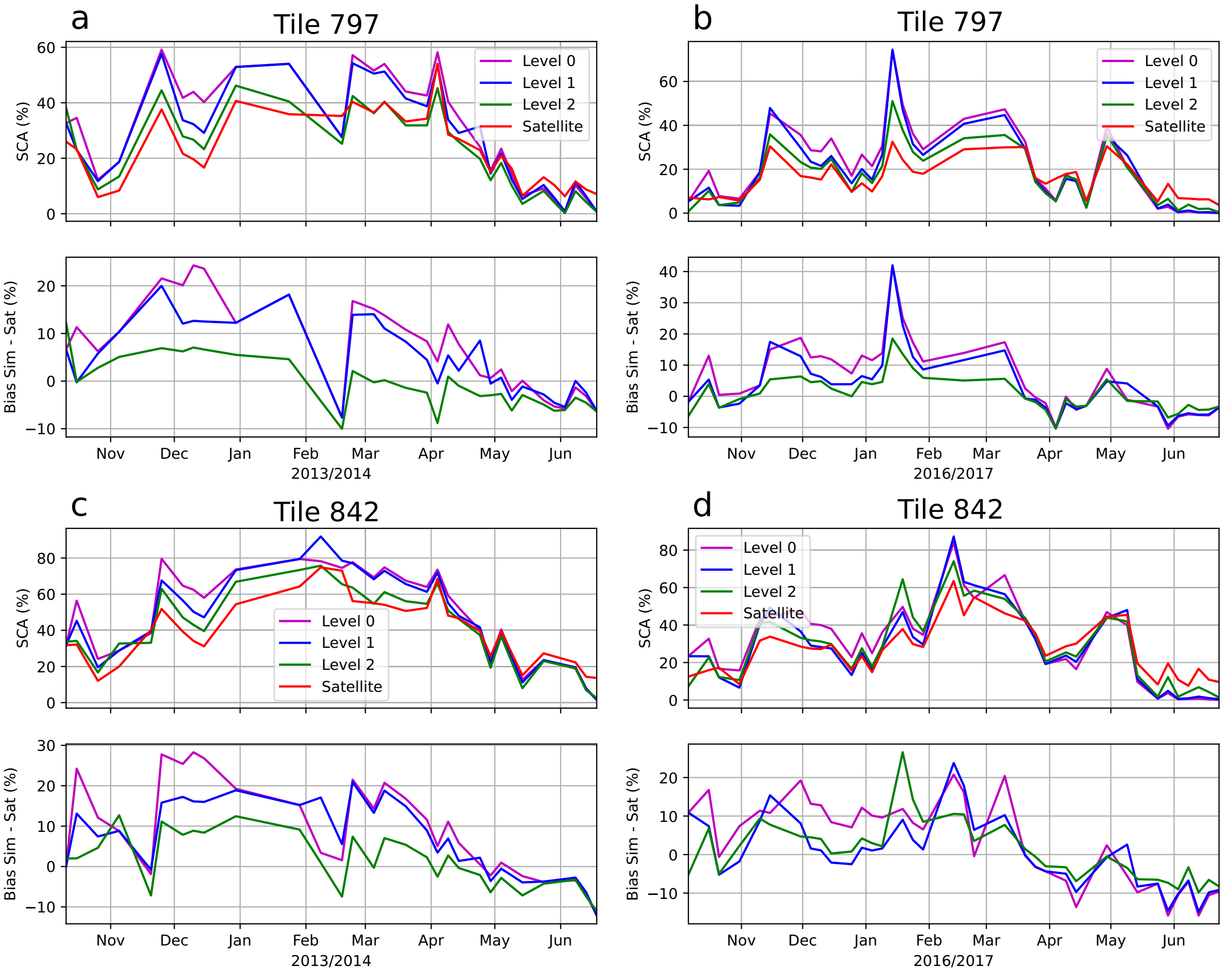

Fig. 10 Percentage SCA and SCA bias with respect to the EO images for: (**a**) Tile 797, year 2013/2014; (**b**) Tile 797, year 2016/2017; (**c**) Tile 842, year 2013/2014; (**d**) Tile 842, year 2016/2017.

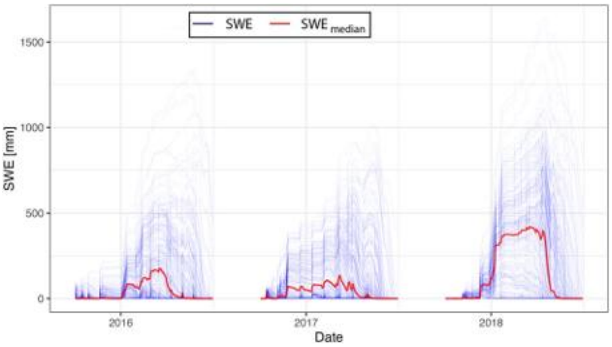

Fig. 11 SWE extracted at some specific locations in the Aosta Valley Region, Po River District as a time series from October 3rd, 2015 to July 1st, 2018. SWE (blue) denotes each selected location in the region, whereas, the SWE_{median} (red) denotes the median of all the locations.

improvements and others slight declines. Such a result comes from the fact that EO data provide information about the snow coverage over a large scale; this information does not automatically translate into a measurement on HS at the point-like scale of the snow gauges.

3. Level 2 simulations (i.e., meteo input + EO data + *in-situ* data assimilation) consistently lead to significant performance improvements at the local scale (i.e., with respect to the *in-situ* snow gauges).

From Fig. 10, the following considerations can be taken:

4. As expected, with only a few exception, the assimilation of EO data (i.e., Level 1) enhances the performance of the simulations at global scale; such a result is highlighted in the "Bias Sim - Sat (%)" panels of Fig. 10, showing the blue line (Level 1 simulation) nearest to the 0 with respect to the magenta line (Level 0);
5. With only a few exceptions, the assimilation of both EO and *in-situ* data (i.e., Level 2) usually further enhance the performance of the simulation; this is clearly visible in the "Bias Sim - Sat (%)" panels of Fig. 10.
6. As reported in Table 9, the comparatively lower values of RMSE (%) and MAE (%) during level 1 and level 2 simulations clearly indicate an overall improvement in the reconstruction of the SCA when assimilating the EO data (i.e., Level 1) and both EO and *in-situ* data (i.e., Level 2), in comparison to the Level 0 simulations.

Based on the reported observations, data consistency can be assumed, because the enhancement in the simulation performance due to the assimilation of *in-situ* data (present in the entire dataset) is more significant than associated with the assimilation of EO-retrieved SCA maps (2002-2021).

Usage Notes

The data is being distributed as a georeferenced temporal raster data and therefore, can be processed and visualised using any Geographic Information System (GIS); furthermore, any programming language with GIS capabilities can be used to analyse and visualise the data. To provide an overview of the data, we extracted a subset between 2015 to 2018 as a time series from the raster data at some selected locations in the Aosta Valley region (Fig. 11). These kind of time series could be a valuable resource for calibrating or validating snow melting models such as temperature index models available in many lumped or semi-distributed models like GEOframe modelling system[33], SWAT[55] or HEC-RAS[56] which all have simple lumped parameter SWE modules. Overall, the length, temporal and spatial resolution of the presented dataset makes it a valuable resource for understanding the snow dynamics in the Po River Basin District and evaluating its impact on the hydrology and the ecosystems downstream, further making possible to consider it as a reference dataset for any estimation of the snow water equivalent estimation in the area.

Code availability

The model used for producing the data is freely available at the following link https://github.com/geotopmodel/geotop and more information about the model[16] and the approach can be found here[6].

Received: 4 June 2024; Accepted: 12 February 2025;

References

1. Hock, R. *et al.* High mountain areas. In Pörtner, H.-O. *et al.* (eds.) *IPCC Special Report on the Ocean and Cryosphere in a Changing Climate*, 131–202, https://doi.org/10.1017/9781009157964.004 (Cambridge University Press, Cambridge, UK and New York, NY, US, 2019).
2. Carrer, M., Dibona, R., Prendin, A. L. & Brunetti, M. Recent waning snowpack in the alps is unprecedented in the last six centuries. *Nat. Clim. Chang.* **13**, 155–160, https://doi.org/10.1038/s41558-022-01575-3 (2023).
3. Beniston, M. *et al.* The european mountain cryosphere: a review of its current state, trends, and future challenges. *Cryosphere* **12**, 759–794, https://doi.org/10.5194/tc-12-759-2018 (2018).

4. Viviroli, D., Dürr, H. H., Messerli, B., Meybeck, M. & Weingartner, R. Mountains of the world, water towers for humanity: Typology, mapping, and global significance. *Water Resour. Res.* 43, https://doi.org/10.1029/2006WR005653 (2007).
5. Immerzeel, W. W. *et al*. Importance and vulnerability of the world's water towers. *Nature* **577**, 364–369, https://doi.org/10.1038/s41586-019-1822-y (2020).
6. Dall'Amico, M., Endrizzi, S. & Tasin, S. Mysnowmaps: operative high-resolution real-time snow mapping. In *International Snow Science Workshop, Innsbruck, Austria*, 328–332, http://arc.lib.montana.edu/snow-science/item/2545 (2018).
7. Dozier, J., Bair, E. H. & Davis, R. E. Estimating the spatial distribution of snow water equivalent in the world's mountains. *WIREs Water* **3**, 461–474, https://doi.org/10.1002/wat2.1140 (2016).
8. Raleigh, M. S. & Small, E. E. Snowpack density modeling is the primary source of uncertainty when mapping basin-wide SWE with lidar. *Geophys. Res. Lett.* **44**, 3700–3709, https://doi.org/10.1002/2016GL071999 (2017).
9. Avanzi, F. *et al*. Learning about precipitation lapse rates from snow course data improves water balance modeling. *Hydrology and Earth System Sciences* **25**, 2109–2131, https://doi.org/10.5194/hess-25-2109-2021 (2021).
10. Avanzi, F. *et al*. It-snow: a snow reanalysis for italy blending modeling, *in-situ* data, and satellite observations (2010–2021). *Earth System Science Data Discussions* **2022**, 1–30, https://doi.org/10.5194/essd-15-639-2023 (2022).
11. Bozzoli, M. *et al*. Long-term snowfall trends and variability in the alps. *International Journal of Climatology* 1–21, https://doi.org/10.1002/joc.8597 (2024).
12. Zakeri, F., Mariethoz, G. & Girotto, M. High-resolution snow water equivalent estimation: A data-driven method for localized downscaling of climate data. *EGUsphere* **2024**, 1–30, https://doi.org/10.5194/egusphere-2024-1943 (2024).
13. Montanari, A. *et al*. Why the 2022 po river drought is the worst in the past two centuries. *Sci Adv* **9**, eadg8304, https://doi.org/10.1126/sciadv.adg8304 (2023).
14. Avanzi, F. *et al*. Winter snow deficit was a harbinger of summer 2022 socio-hydrologic drought in the po basin, italy. *Communications Earth & Environment* **5**, 1–12, https://doi.org/10.1038/s43247-024-01222-z (2024).
15. Bavay, M. & Egger, T. Meteoio 2.4. 2: a preprocessing library for meteorological data. *Geoscientific Model Development* **7**, 3135–3151, https://doi.org/10.5194/gmd-7-3135-2014 (2014).
16. Endrizzi, S., Gruber, S., Dall'Amico, M. & Rigon, R. GEOtop 2.0: simulating the combined energy and water balance at and below the land surface accounting for soil freezing, snow cover and terrain effects. *Geosci. Model Dev.* **7**, 2831–2857, https://doi.org/10.5194/gmd-7-2831-2014 (2014).
17. Rigon, R., Bertoldi, G. & Over, T. M. GEOtop: A distributed hydrological model with coupled water and energy budgets. *J. Hydrometeorol.* **7**, 371–388, https://doi.org/10.1175/JHM497.1 (2006).
18. Irigoin, F. Tiling. In Padua, D. (ed.) *Encyclopedia of Parallel Computing*, 2040–2049, https://doi.org/10.1007/978-0-387-09766-4_511 (Springer US, Boston, MA, 2011).
19. Muñoz-Sabater, J. *et al*. ERA5-Land: a state-of-the-art global reanalysis dataset for land applications. *Earth Syst. Sci. Data* **13**, 4349–4383, https://doi.org/10.5194/essd-13-4349-2021 (2021).
20. Matiu, M. *et al*. Observed snow depth trends in the european alps 1971 to 2019. *The Cryosphere Discussions* **2020**, 1–50, https://doi.org/10.5194/tc-15-1343-2021 (2020).
21. Notarnicola, C. *et al*. Snow cover maps from MODIS images at 250 m resolution, part 1: Algorithm description. *Remote Sensing* **5**, 110–126, https://doi.org/10.3390/rs5010110 (2013).
22. Notarnicola, C. *et al*. Snow cover maps from MODIS images at 250 m resolution, part 2: Validation. *Remote Sensing* **5**, 1568–1587, https://doi.org/10.3390/rs5041568 (2013).
23. Józsa, E., Fábián, S. Á. & Kovács, M. An evaluation of eu-dem in comparison with aster gdem, srtm and contour-based dems over the eastern mecsek mountains. *Hungarian Geographical Bulletin* **63**, 401–423, https://doi.org/10.15201/hungeobull.63.4.3 (2014).
24. Hunziker, S. *et al*. Identifying, attributing, and overcoming common data quality issues of manned station observations. *Int. J. Climatol.* **37**, 4131–4145, https://doi.org/10.1002/joc.5037 (2017).
25. Nicholson, L. I., Prinz, R., Mölg, T. & Kaser, G. Micrometeorological conditions and surface mass and energy fluxes on lewis glacier, mt kenya, in relation to other tropical glaciers. *Cryosphere* **7**, 1205–1225, https://doi.org/10.5194/tc-7-1205-2013 (2013).
26. Goodison, B. E., Louie, P. Y. & Yang, D. Wmo solid precipitation measurement intercomparison. Tech. Rep., World Meteorological Organization Geneva, Switzerland https://library.wmo.int/idurl/4/28336 (1998).
27. Henn, B., Raleigh, M. S., Fisher, A. & Lundquist, J. D. A comparison of methods for filling gaps in hourly Near-Surface air temperature data. *J. Hydrometeorol.* **14**, 929–945, https://doi.org/10.1175/JHM-D-12-027.1 (2013).
28. Chen, F.-W. & Liu, C.-W. Estimation of the spatial rainfall distribution using inverse distance weighting (idw) in the middle of taiwan. *Paddy and Water Environment* **10**, 209–222, https://doi.org/10.1007/s10333-012-0319-1 (2012).
29. Liston, G. E. & Elder, K. A meteorological distribution system for high-resolution terrestrial modeling (MicroMet). *J. Hydrometeorol.* **7**, 217–234, https://doi.org/10.1175/JHM486.1 (2006).
30. Zanotti, F., Endrizzi, S., Bertoldi, G. & Rigon, R. The geotop snow module. *Hydrological Processes* **18**, 3667–3679, https://doi.org/10.1002/hyp.5794 (2004).
31. Engel, M., Notarnicola, C., Endrizzi, S. & Bertoldi, G. Snow model sensitivity analysis to understand spatial and temporal snow dynamics in a high-elevation catchment. *Hydrological processes* **31**, 4151–4168, https://doi.org/10.1002/hyp.11314 (2017).
32. Endrizzi, S. *et al*. Snow cover patterns and evolution at basin scale: Geotop model simulations and remote sensing observations. In *Eastern Snow Conference*, 195–209, https://hdl.handle.net/11572/59569 ([easternsnow], 2006).
33. Formetta, G., Kampf, S. K., David, O. & Rigon, R. Snow water equivalent modeling components in NewAge-JGrass. *Geoscientific Model Development* **7**, 725–736, https://doi.org/10.5194/gmd-7-725-2014 (2014).
34. Gubler, S., Endrizzi, S., Gruber, S. & Purves, R. S. Sensitivities and uncertainties of modeled ground temperatures in mountain environments. *Geoscientific Model Development* **6**, 1319–1336, https://doi.org/10.5194/gmd-6-1319-2013 (2013).
35. Rasmussen, R. *et al*. How well are we measuring snow: The NOAA/FAA/NCAR winter precipitation test bed. *Bull. Am. Meteorol. Soc.* **93**, 811–829, https://doi.org/10.1175/BAMS-D-11-00052.1 (2012).
36. Farinotti, D., Usselmann, S., Huss, M., Bauder, A. & Funk, M. Runoff evolution in the swiss alps: Projections for selected high-alpine catchments based on ensembles scenarios. *Hydrological Processes* **26**, 1909–1924, https://doi.org/10.1002/hyp.8276 (2012).
37. Schöber, J. *et al*. Snow cover characteristics in a glacierized catchment in the tyrolean alps-improved spatially distributed modelling by usage of lidar data. *Journal of Hydrology* **519**, 3492–3510, https://doi.org/10.1016/j.jhydrol.2013.12.054 (2014).
38. Hanzer, F., Helfricht, K., Marke, T. & Strasser, U. Multilevel spatiotemporal validation of snow/ice mass balance and runoff modeling in glacierized catchments. *Cryosphere* **10**, 1859–1881, https://doi.org/10.5194/tc-10-1859-2016 (2016).
39. Mair, E. *et al*. A simple method to combine snow height and meteorological observations to estimate winter precipitation at sub-daily resolution. *Hydrol. Sci. J.* **61**, 2050–2060, https://doi.org/10.1080/02626667.2015.1081203 (2016).
40. Valt, M. *et al*. Predicting new snow density in the italian alps: A variability analysis based on 10 years of measurements. *Hydrological processes* **32**, 3174–3187, https://doi.org/10.1002/hyp.13249 (2018).
41. Števuliáková, P. & Hurtik, P. Intersection over union with smoothing for bounding box regression. In *Advances in Computational Intelligence*, 206–216, https://doi.org/10.1007/978-3-031-43078-7_17 (Springer, 2023).
42. Rezatofighi, H. *et al*. Generalized intersection over union: A metric and a loss for bounding box regression. In *Proceedings of the IEEE/CVF conference on computer vision and pattern recognition*, 658–666, https://doi.org/10.1109/CVPR.2019.00075 (2019).
43. Choi, H., Lee, H.-J., You, H.-J., Rhee, S.-Y. & Jeon, W.-S. Comparative analysis of generalized intersection over union and error matrix for vegetation cover classification assessment. *Sensors & Materials* **31**, https://doi.org/10.18494/SAM.2019.2584 (2019).

44. Chen, P., Zhou, H., Li, Y., Liu, B. & Liu, P. Shape similarity intersection-over-union loss hybrid model for detection of synthetic aperture radar small ship objects in complex scenes. *IEEE Journal of Selected Topics in Applied Earth Observations and Remote Sensing* **14**, 9518–9529, https://doi.org/10.1109/JSTARS.2021.3112469 (2021).
45. Pernov, J. B., Gros-Daillon, J. & Schmale, J. Comparison of selected surface level ERA5 variables against *in-situ* observations in the continental Arctic. *Q. J. R. Meteorol. Soc.* **150**, 2123–2146, https://doi.org/10.1002/qj.4700 (2024).
46. Dall'Amico, M. *et al.* Snow Water Equivalent Dataset in the Po River District, Italy. *Zenodo*, https://doi.org/10.5281/zenodo.11196628 (2024).
47. Nash, J. E. & Sutcliffe, J. V. River flow forecasting through conceptual models part I — a discussion of principles. *J. Hydrol.* **10**, 282–290, https://doi.org/10.1016/0022-1694(70)90255-6 (1970).
48. Gupta, H. V., Kling, H., Yilmaz, K. K. & Martinez, G. F. Decomposition of the mean squared error and NSE performance criteria: Implications for improving hydrological modelling. *J. Hydrol.* **377**, 80–91, https://doi.org/10.1016/j.jhydrol.2009.08.003 (2009).
49. Günther, D., Marke, T., Essery, R. & Strasser, U. Uncertainties in snowpack simulations—assessing the impact of model structure, parameter choice, and forcing data error on point-scale energy balance snow model performance. *Water Resour. Res.* **55**, 2779–2800, https://doi.org/10.1029/2018WR023403 (2019).
50. Yang, K. *et al.* Combining ground-based and remotely sensed snow data in a linear regression model for real-time estimation of snow water equivalent. *Adv. Water Resour.* **160**, 104075, https://doi.org/10.1016/j.advwatres.2021.104075 (2022).
51. Günther, D., Hanzer, F., Warscher, M., Essery, R. & Strasser, U. Including parameter uncertainty in an intercomparison of physically-based snow models. *Front. Earth Sci.* 8, https://doi.org/10.3389/feart.2020.542599 (2020).
52. Essery, R., Morin, S., Lejeune, Y. & B Ménard, C. A comparison of 1701 snow models using observations from an alpine site. *Adv. Water Resour.* **55**, 131–148, https://doi.org/10.1016/j.advwatres.2012.07.013 (2013).
53. Hou, J., Huang, C., Chen, W. & Zhang, Y. Improving snow estimates through assimilation of MODIS fractional snow cover data using machine learning algorithms and the common land model. *Water Resour. Res.* **57**, https://doi.org/10.1029/2020WR029010 (2021).
54. Zappa, M. Objective quantitative spatial verification of distributed snow cover simulations—an experiment for the whole of switzerland / vérification quantitative spatiale objective de simulations distribuées de la couche de neige—une étude pour l'ensemble de la suisse. *Hydrol. Sci. J.* **53**, 179–191, https://doi.org/10.1623/hysj.53.1.179 (2008).
55. Arnold, J. G. *et al.* SWAT: Model use, calibration, and validation. *Trans. ASABE* **55**, 1491–1508, https://doi.org/10.13031/2013.42256 (2012).
56. Brunner, G. W. *HEC river analysis system (HEC-RAS)*. 147 (US Army Corps of Engineers, Hydrologic Engineering Center, 1994).

Acknowledgements

The reconstruction of the Snow Water Equivalent maps related to the Po River District has been funded by the GCU-M (Gruppo di Coordinamento Unificato-Magre), in which the National Civil Protection Department (DPC), the Interregional Agency for the Po River (AIPo), the Emilia-Romagna Region, the Lombardy Region, the Piedmont Region, the Valle d'Aosta Region and the Veneto Region participate, in addition to the Po River Basin District Authority (AdBPo). For providing the data needed to produce the maps, we would like to thank: Arpae - Agenzia regionale per la prevenzione, l'ambiente e l'energia dell'Emilia-Romagna-STRUTTURA IDRO-METEO-CLIMA; ARPA Lombardia-Agenzia regionale per la protezione dell'ambiente della Lombardia-Settore Rischi Naturali, Clima e Usi Sostenibili delle Acque- U.O.C. Servizio Idro-Nivo-Meteo e Clima; ARPA Piemonte-Agenzia Regionale per la Protezione Ambientale del Piemonte-Dipartimento Rischi Naturali e Ambientali-Idrologia e Qualitá delle Acque; Regione autonoma Valle d'Aosta-Dipartimento protezione civile e vigili del fuoco-Centro Funzionale regionale; Provincia autonoma di Trento-Dipartimento Protezione Civile-Servizio Prevenzione Rischi-Ufficio Previsioni e Pianificazione; Eurac Research; MeteoSwiss, Federal Office for Meteorology and Climatology; WSL Institute for Snow and Avalanche Research SLF- Service de données (https://doi.org/10.16904/envidat.408, https://doi.org/10.16904/envidat.406); METEO FRANCE-Division Valorisation des Données, METEOMONT CARABINIERI (data generated for regional avalanche hazard assessment according to European EAWS standards). The work of J.M.W. has been funded by Fondazione CARITRO Cassa di Risparmio di Trento e Rovereto, grant number 2022.0246. R.R and J.M.W. would like to thank and acknowledge the funding from the European Union under NextGenerationEU. PRIN 2022 Prot. n. 202295PFKP. The J-snow methodology has been developed and funded under the European Space Agency (ESA) eo4alps snow (https://www.waterjade.com/en/eo4alps-snow/) project. The EO-data assimilation has been improved through the ESA-funded projects Digital Twin of Alps (DTA) (https://digitaltwinalps.com/) (contract number 4000139281/22/I-DT) and 4DHydro (https://4dhydro.eu/) (contract number ESA AO/1-11298/22/I-EF). J-snow has been awarded by the myEUspace 2023 Competition award (https://www.euspa.europa.eu/newsroom-events/news) funded by the EU Agency for the Space Programme (EUSPA).

Author contributions

Conceptualization (All Authors), Writing - Original draft (J.M.W., R.R.), Methodology (M.D., S.T., F.D.P.), Writing - review and editing (M.D., S.T., F.D.P., M.B., G.F., G.R., R.R., J.M.W.), Funding acquisition (F.T., M.B., P.L., R.R.), Formal analysis (M.D., S.T., F.D.P., J.M.W., G.R.), Visualisation (M.D., S.T., F.D.P, J.M.W.), Data collection (M.B.). All the authors contributed in editing and reviewing the manuscript. All the authors contributed to the project design and scope.

Competing interests

The authors declare no competing interests.

Additional information

Correspondence and requests for materials should be addressed to J.M.W.